

Dynamic Terahertz Beamforming Based on Magnetically Switchable Hyperbolic Materials

William O. F. Carvalho^{1,*}, E. Moncada-Villa², J. R. Mejía-Salazar³, and Danilo H. Spadoti¹

¹*Federal University of Itajubá (UNIFEI), 37500-903 Itajubá, MG, Brazil.*

²*Escuela de Física, Universidad Pedagógica y Tecnológica de Colombia, Avenida Central del Norte 39-115, Tunja, Colombia*

³*National Institute of Telecommunications (Inatel), Santa Rita do Sapucaí, MG, 37540-000, Brazil*

(Dated: October 11, 2023)

In this work, we introduce a concept to enable dynamic beamforming of terahertz (THz) wavefronts using applied magnetic fields (\mathbf{B}). The proposed system exploits the magnetically switchable hyperbolic dispersion of the InSb semiconductor. This phenomenology, combined with diffractive surfaces and magnetic tilting of scattered fields, allows the design of a metasurface that works with either circularly or linearly polarized wavefronts. In particular, we demonstrate numerically that the transmitted beam tilting can be manipulated with the direction and magnitude of \mathbf{B} . Numerical results, obtained through the finite element method (FEM), are qualitatively supported by semi-analytical results from the generalized dipole theory. Motivated by potential applications in future Tera-WiFi active links, a proof of concept is conducted for the working frequency $f = 300$ GHz. The results indicate that the transmitted field can be actively tuned to point in five different directions with beamforming of $\pm 45^\circ$, depending on the magnitude and direction of \mathbf{B} . In addition to magnetic beamforming, we also demonstrate that our proposal exhibits magnetic circular dichroism (MCD), which can also find applications in magnetically tunable THz isolators for one-way transmission/reflection.

I. INTRODUCTION

The electromagnetic gap between electronic and optical regimes, widely-known as the terahertz (THz) band (from 0.1 THz to 10 THz), has been drawing increasing attention during the last years. Such interest is mainly driven by a plethora of applications, including spectroscopy,¹ imaging,² security,³ sensing,⁴ and communications,^{5–12} among others. The first challenge the researchers tackled was the development of THz sources and detectors, which today are consolidated into a number of different approaches and commercially available devices.¹³ Nevertheless, these THz equipments are passive and therefore exhibit limited functionalities. For example, the need to use highly directional beams in THz wireless broadcasting (generated from high-gain antennas designed to surpass the large free-space path loss¹⁴) restricts communication to two fixed points, called the transmit and receive antennas. Thus, researchers are currently focused on finding mechanisms/alternatives that allow active manipulation of THz wavefronts. A promising approach to achieve the latter goal is the use of metasurfaces¹⁵ (i.e. artificial materials comprising two-dimensional arrays of sub-wavelength “meta-atoms”) engineered to dictate (at will) reflectance, transmittance, and absorbance features.¹⁶ Although metasurfaces operating in the microwave and optical regimes can be actively manipulated using diodes (e.g. varactors)^{17,18} and tunable light-matter interactions,^{19–21} respectively, innovative approaches are still needed for the THz range. Some attempts include the use of liquid crystals^{22–25} and phase-change materials.^{26–28} However, these latest platforms require precise control of the temperature of the building materials, hindering large-scale implementation for terahertz systems. Moreover,

temperature changes conventionally occur at low speeds, thus limiting the velocity of operation. Hence, the search for fast and dynamic beamforming of THz wavefronts with large-scale implementable solutions remains an open problem.

Inspired by the use of magnetic fields to manipulate the optical radiated beams from magnetoplasmonic nanoantennas,^{29–31} we hypothesized that magnetic fields can also be employed for dynamic THz beamforming through magnetically tunable metasurfaces. In the THz range, Faraday and polar magneto-optical (MO) Kerr effects (PMOKE) were recently used for isolators and filters. These achievements have been made using MO metasurfaces comprising the InSb material,^{32–35} whose conduction electrons are strongly affected by applied magnetic fields. Nevertheless, Faraday and PMOKE phenomena only induce polarization rotation effects, which do not tilt the transmitted/radiated beams, as demonstrated analytically and numerically in Ref. [31]. Moreover, it is well-known from the first observations of MO phenomena by Faraday³⁶ and Kerr^{37,38} that the Faraday and PMOKE effects are at least one order of magnitude higher than their in-plane counterparts, i.e., the longitudinal and transverse MO Kerr effects (LMOKE and TMOKE). Therefore, configurations different to Faraday and PMOKE are conventionally studied in the visible and infrared wavelength ranges, where strong light-matter interactions are used to enhance their amplitudes.³⁹

In this work, we demonstrate a magnetically active metasurface that allows the dynamic beamforming of THz wavefronts. Our proposal consists of a fishnet-like metasurface made of aluminum (Al) and the indium antimonide (InSb) semiconducting material, as illustrated in Figure 1. The inset of this figure shows a cross of Al mate-

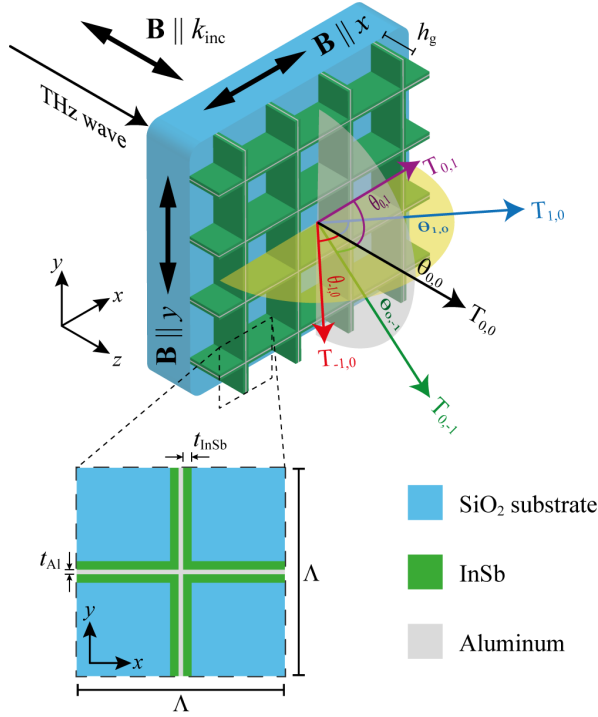


Figure 1: Schematic of the MO metasurface. The inset shows the material composition and geometrical parameters of the unit cell.

rial symmetrically covered by a thin film of InSb on each side. The Al is a metallic material conventionally used in the fabrication of resonant THz metasurfaces. Indeed, the cross-like design of Al elements can be easily found in recent works.⁴⁰ Hence, we focused here on exploiting the MO activity of the InSb material (which can be deposited over the entire surface and then molded using ion-milling and focused ion beam (FIB) techniques⁴¹ for the active manipulation of THz wavefronts. In particular, the InSb material exhibits a magnetically switchable hyperbolic dispersion, i.e., the regular to hyperbolic dispersion can be activated/deactivated using a static magnetic field.⁴² The later feature, in combination with geometric design, is used to allow the excitation of asymmetric dipole resonances when the direction of the in-plane magnetic field is flipped. These asymmetric resonances dictate the preferred diffraction order (± 1) for the transmitted wavefronts, as qualitatively demonstrated using the dipole theory for the unit cell.

II. METHODOLOGY

A metasurface composed of a two-dimensional periodic arrangement of metallic crosses (made of Al) is considered, as depicted in the inset of Figure 1. The period length (Λ) and thickness (t_{Al}) of the crosses are selected to resonate at the THz frequency range. Since the frequency $f = 300$ GHz has applicability for future wireless

communications,^{43,44} we used it as the working frequency to prove our concept. MO activity is introduced in the system by using uniform and symmetrically placed slabs of InSb material on each side of the metal building blocks (see the inset of Figure 1). The InSb slabs have a thickness t_{InSb} and the same height of the Al crosses, i.e., h_g according to Figure 1. The structure, which can be fabricated by a combination of different techniques,^{40,41} is considered grown on a conventional SiO_2 substrate. Under the effect of an externally applied magnetic field, the off-diagonal components of the InSb material have non-zero values. For the magnetic field (\mathbf{B}) pointing along one of the main axis, we have

$$\tilde{\epsilon}_{\text{InSb}} = \begin{pmatrix} \epsilon_{\parallel} & 0 & 0 \\ 0 & \epsilon_{\perp} & i\epsilon_{\text{off}} \\ 0 & -i\epsilon_{\text{off}} & \epsilon_{\perp} \end{pmatrix}, \quad (1)$$

for \mathbf{B} parallel to the x -axis,

$$\tilde{\epsilon}_{\text{InSb}} = \begin{pmatrix} \epsilon_{\perp} & 0 & i\epsilon_{\text{off}} \\ 0 & \epsilon_{\parallel} & 0 \\ -i\epsilon_{\text{off}} & 0 & \epsilon_{\perp} \end{pmatrix}, \quad (2)$$

for \mathbf{B} along the y -axis and

$$\tilde{\epsilon}_{\text{InSb}} = \begin{pmatrix} \epsilon_{\perp} & i\epsilon_{\text{off}} & 0 \\ -i\epsilon_{\text{off}} & \epsilon_{\perp} & 0 \\ 0 & 0 & \epsilon_{\parallel} \end{pmatrix}, \quad (3)$$

for \mathbf{B} applied along the z -axis. The permittivities ϵ_{\perp} , ϵ_{\parallel} , and ϵ_{off} are described by

$$\epsilon_{\perp} = \epsilon_{\infty} - \frac{\omega_p^2 (\omega + i\gamma)}{\omega [(\omega + i\gamma)^2 - \omega_c^2]}, \quad (4)$$

$$\epsilon_{\parallel} = \epsilon_{\infty} - \frac{\omega_p^2}{\omega(\omega + i\gamma)}, \quad (5)$$

$$\epsilon_{\text{off}} = -\frac{\omega_p^2 \omega_c}{\omega [(\omega + i\gamma)^2 - \omega_c^2]}, \quad (6)$$

where the subscripts \parallel and \perp are used to indicate the permittivity components that are parallel and perpendicular to \mathbf{B} , respectively. ϵ_{∞} is the high frequency permittivity and $\omega_p = \sqrt{Ne^2/\epsilon_0 m^*}$ is the plasma frequency. N represents the carrier density, e the electron charge, ϵ_0 the vacuum permittivity and $m^* = 0.014m$ the electron effective mass for the InSb material. ω is the angular frequency, $\gamma = e/\mu m^*$ is the damping constant, μ is the carrier mobility, and $\omega_c = eB/m^*$ ($B = |\mathbf{B}|$) is the cyclotron frequency. Since N is strongly temperature-dependent, we employed an empirical equation from the available literature $N = 5.76 \times 10^{14} \times T_K^{1.5} \exp\left(\frac{-1.5 \times 10^3}{T_K}\right)$,⁴⁵ where T_K is the temperature in Kelvin. The permittivities (considered isotropic) of Al and SiO_2 were taken from the available experimental literature.^{46,47}

The grating features of the proposed metasurface provide different orders and efficiencies for diffractively transmitted fields ($T_{m,n}$), as depicted by arrows in Figure 1.

As we are using a symmetric two-dimensional grating ($\Lambda_x = \Lambda_y = \Lambda$), the corresponding phase-matching condition for normal incidence is expressed by⁴⁸

$$m^2 + n^2 = \frac{\Lambda^2 \sin^2 \theta_{m,n}}{\lambda^2} \quad (7)$$

where m and n are integer numbers representing the diffraction orders, with diffracted angle $\theta_{m,n}$. Since we are showing a proof-of-concept for future wireless THz broadcasting, we focused only (for simplicity) on transmitted diffraction orders with $\theta_{m,n} = 45^\circ$ for $(m, n) = (0, \pm 1)$ and $(m, n) = (\pm 1, 0)$. Thus, we set $\Lambda = 1414 \mu\text{m}$, according to Eq. (7), to allow only orders 0th and 1st to be transmitted.

Full-wave numerical simulations were carried out using the finite element method (FEM), within the commercial software COMSOL Multiphysics[®]. Refined irregular-mesh-sizes were used for improved precision, with finer meshes near the boundaries of the grating. Floquet periodic boundary conditions were used along the x - and y -axes, whereas absorbing perfectly matched layers (PMLs) were considered along the z -boundaries. All results were obtained for normal incident THz fields, with a frequency $f = 300 \text{ GHz}$.

In addition to full-wave numerical simulations, semi-analytical results were obtained within the discrete dipole

approximation (DDA)⁴⁹, where we consider a system of N MO point dipoles, at arbitrary positions \mathbf{r}_i , having polarizabilities

$$\hat{\alpha}_i = \left(\hat{\mathbf{1}} - i \frac{k^3}{6\pi} \hat{\alpha}_{i,0} \right)^{-1} \hat{\alpha}_{i,0}, \quad (8)$$

with $\hat{\alpha}_{i,0} = 3v_i[\hat{\epsilon}_i - \hat{\mathbf{1}}][\hat{\epsilon}_i + 2\hat{\mathbf{1}}]^{-1}$ for the static (non-radiative) polarizability, where v_i and $\hat{\epsilon}_i$ are the volume and dielectric permittivity tensor of each dipole, respectively. Under the excitation of a monochromatic electromagnetic plane wave, the scattered electric and magnetic fields (at a position \mathbf{r}) can be expressed as^{49–51}

$$\mathbf{E}(\mathbf{r}) = \frac{k^2}{\varepsilon_0} \bar{G}^E \cdot \bar{\mathbf{p}}, \quad (9)$$

$$\mathbf{H}(\mathbf{r}) = \frac{k^2}{\varepsilon_0} \bar{G}^H \cdot \bar{\mathbf{p}}, \quad (10)$$

where $k = \omega/c$ is wave vector magnitude of the emitted radiation with angular frequency ω (c is the speed of light in vacuum). $\bar{G}^\beta = (\hat{G}^\beta(\mathbf{r}, \mathbf{r}_1), \hat{G}^\beta(\mathbf{r}, \mathbf{r}_2), \dots, \hat{G}^\beta(\mathbf{r}, \mathbf{r}_N))$ (with β representing E or H) are $3 \times 3N$ matrices built with the following electric and magnetic dyadic Green's functions

$$\hat{G}^E(\mathbf{r}, \mathbf{r}_i) = \frac{e^{ikR_i}}{4\pi R_i} \left[\left(1 + \frac{ikR_i - 1}{(kR_i)^2} \right) \hat{\mathbf{1}} + \left(\frac{3 - 3ikR_i - (kR_i)^2}{(kR_i)^2} \right) \hat{\mathbf{R}}_i \otimes \hat{\mathbf{R}}_i \right] \quad (11)$$

$$\hat{G}^H(\mathbf{r}, \mathbf{r}_i) = \frac{e^{ikR_i}}{4\pi Z_0 R_i} \left(1 + \frac{i}{kR_i} \right) \times \begin{pmatrix} 0 & z - z_i & -(y - y_i) \\ -(z - z_i) & 0 & x - x_i \\ y - y_i & -(x - x_i) & 0 \end{pmatrix}, \quad (12)$$

where $Z_0 = \sqrt{\mu_0/\varepsilon_0}$ is the vacuum electromagnetic impedance, $\mathbf{R}_i = \mathbf{r} - \mathbf{r}_i$, $R_i = |\mathbf{R}_i|$, and $\hat{\mathbf{R}}_i = \mathbf{R}_i/R_i$.

The $3N \times 1$ supervector $\bar{\mathbf{p}} = (\mathbf{p}_1, \mathbf{p}_2, \dots, \mathbf{p}_N)^T$, in Equations (9) and (10), contains the dipolar moments $\mathbf{p}_i = \varepsilon_0 \hat{\alpha}_i \mathbf{E}_{\text{exc},i}$ of the system. Then, we can write

$$\bar{\mathbf{p}} = \varepsilon_0 \bar{\alpha} \bar{\mathbf{E}}_{\text{exc}}, \quad (13)$$

where $\bar{\alpha} = \text{diag}(\hat{\alpha}_1, \hat{\alpha}_2, \dots, \hat{\alpha}_N)$ and $\bar{\mathbf{E}}_{\text{exc}} = (\mathbf{E}_{\text{exc},1}, \mathbf{E}_{\text{exc},2}, \dots, \mathbf{E}_{\text{exc},N})^T$ is a $3N \times 1$ supervector comprising the fields that excite all the dipoles in the system. These exciting fields can be determined by a set of N equations of the form⁵²

$$\mathbf{E}_{\text{exc},i} = \mathbf{E}_{\text{inc},i} + k_0^2 \sum_{j \neq i} \hat{G}_{ji} \hat{\alpha}_j \mathbf{E}_{\text{exc},i}, \quad (14)$$

where $\mathbf{E}_{\text{inc},i} = \mathbf{E}_0 e^{i(\mathbf{k} \cdot \mathbf{r}_i - \omega t)}$ is the incident field upon the i -th dipole, and $\hat{G}_{ji} = \hat{G}_{ji}(\mathbf{r}_j, \mathbf{r}_i)$ is the inter-dipolar

Green's function, given by

$$\hat{G}(\mathbf{r}_j, \mathbf{r}_i) = \frac{e^{ikR_{ji}}}{4\pi R_{ji}} \left[\left(1 + \frac{ikR_{ji} - 1}{(kR_{ji})^2} \right) \hat{\mathbf{1}} + \left(\frac{3 - 3ikR_{ji} - (kR_{ji})^2}{(kR_{ji})^2} \right) \hat{\mathbf{R}}_{ji} \otimes \hat{\mathbf{R}}_{ji} \right], \quad (15)$$

with $\mathbf{R}_{ji} = \mathbf{r}_j - \mathbf{r}_i$. The latter system of equations can be expressed compactly as

$$\bar{\mathbf{E}}_{\text{exc}} = \bar{T} \bar{\mathbf{E}}_{\text{inc}}, \quad (16)$$

where $\bar{T} = (\hat{\mathbf{1}} - k_0^2 \Delta \bar{G} \bar{\alpha})^{-1}$ and $\Delta \bar{G} = \bar{G} - \text{diag}\{\bar{G}\}$ are $3N \times 3N$ matrices, with $[\bar{G}]_{ij} = \hat{G}_{ij}$. Therefore, using the Equations (13) and (16), we can rewrite the scattered electric and magnetic fields as

$$\mathbf{E}(\mathbf{r}) = k^2 \bar{G}^E \bar{\alpha} \bar{T} \bar{\mathbf{E}}_{\text{inc}}, \quad (17)$$

$$\mathbf{H}(\mathbf{r}) = k^2 \bar{G}^H \bar{\alpha} \bar{T} \bar{\mathbf{E}}_{\text{inc}}, \quad (18)$$

from where the scattered power per unit area $\mathbf{S}(\mathbf{r}) = \frac{1}{2}\text{Re}\{\mathbf{E}(\mathbf{r}) \times \mathbf{H}^*(\mathbf{r})\}$ can be calculated.

In the case of two identical dipoles, as it is being considered in this work (for simplicity), the expressions above can be reduced to

$$\mathbf{E}(\mathbf{r}) = k^2 \hat{G}^E(\mathbf{r}, \mathbf{r}_1) \hat{\alpha} [\hat{T}_{11} \mathbf{E}_{\text{inc}}(\mathbf{r}_1) + \hat{T}_{12} \mathbf{E}_{\text{inc}}(\mathbf{r}_2)] + k^2 \hat{G}^E(\mathbf{r}, \mathbf{r}_2) \hat{\alpha} [\hat{T}_{21} \mathbf{E}_{\text{inc}}(\mathbf{r}_1) + \hat{T}_{22} \mathbf{E}_{\text{inc}}(\mathbf{r}_2)], \quad (19)$$

$$\mathbf{H}(\mathbf{r}) = k^2 \hat{G}^H(\mathbf{r}, \mathbf{r}_1) \hat{\alpha} [\hat{T}_{11} \mathbf{E}_{\text{inc}}(\mathbf{r}_1) + \hat{T}_{12} \mathbf{E}_{\text{inc}}(\mathbf{r}_2)] + k^2 \hat{G}^H(\mathbf{r}, \mathbf{r}_2) \hat{\alpha} [\hat{T}_{21} \mathbf{E}_{\text{inc}}(\mathbf{r}_1) + \hat{T}_{22} \mathbf{E}_{\text{inc}}(\mathbf{r}_2)], \quad (20)$$

with

$$\hat{T}_{11} = (\hat{\mathbf{I}} - k^4 \hat{G}_{12} \hat{\alpha} \hat{G}_{12} \hat{\alpha})^{-1}, \quad (21)$$

$$\hat{T}_{12} = k^2 \hat{T}_{11} \hat{G}_{12} \hat{\alpha}, \quad (22)$$

$$\hat{T}_{21} = k^2 \hat{G}_{12} \hat{\alpha} \hat{T}_{11}, \quad (23)$$

$$\hat{T}_{22} = \hat{\mathbf{I}} + k^4 \hat{G}_{12} \hat{\alpha} \hat{T}_{11} \hat{G}_{12} \hat{\alpha}, \quad (24)$$

from where numerical results for the scattered energy were calculated.

III. RESULTS AND DISCUSSION

Let us first discuss the permittivity values for the InSb material at $f = 300$ GHz and $T_K = 200$ K, summarized in Table I. For $B = 0$ T we have an isotropic ($\varepsilon_{\parallel} = \varepsilon_{\perp}$ and $\varepsilon_{\text{off}} = 0$) metallic behavior, whilst for $B = \pm 3$ T the InSb material behaves as a HMM,⁵³ i.e., $\varepsilon_{\perp} \varepsilon_{\parallel} < 0$. In particular, the unique feature of having $\varepsilon_{\perp} > 0$ makes InSb slabs behave like high-refractive-index (HRI) dielectric media along those specific directions, which we exploit to produce magnetically tunable dipolar resonances. The latter produces an effect analogous to the case of nanoantennas,^{29–31} but in each unit cell of the metasurface. Therefore, we must find the geometric parameters at which the collective effects, through the constructive phase interference, produce the maximum beamforming. These parameters were found (using the optimization technique in COMSOL) as $t_{\text{InSb}} = 58 \mu\text{m}$, $t_{\text{Al}} = 30 \mu\text{m}$, $h_g = 1000 \mu\text{m}$ and $\Lambda = 1414 \mu\text{m}$, which are considered constant along the entire work.

Figure 2 shows the transmitted diffraction orders $T_{m,n}$, for a linearly polarized (LP) THz wave, as function of the externally applied magnetic field B . To illustrate the symmetry effects of the square unit cell, we calculate $T_{m,n}$ for two different electric field polarizations of the

Table I: Components of ε_{Al} ,⁴⁶ $\varepsilon_{\text{SiO}_2}$ ⁴⁷ and $\tilde{\varepsilon}_{\text{InSb}}$ ⁴⁵ at $f = 300$ GHz and $T_K = 200$ K, under the influence of B .

Parameter	Value	Parameter	Value
ε_{Al}	$-8.08\text{e}5 + i1.95\text{e}6$	$\varepsilon_{\text{SiO}_2}$	$3.8 + i0.02$
ε_{∞}	15.68	ε_{\parallel}	$-31.21 + i20.73$
$\varepsilon_{\perp}, B = 0$ T	$-31.21 + i20.73$	$\varepsilon_{\text{off}}, B = 0$ T	0
$\varepsilon_{\perp}, B = +3$ T	$15.82 + i0.06$	$\varepsilon_{\text{off}}, B = +3$ T	$-2.81 - i0.006$
$\varepsilon_{\perp}, B = -3$ T	$15.82 + i0.06$	$\varepsilon_{\text{off}}, B = -3$ T	$2.81 + i0.006$

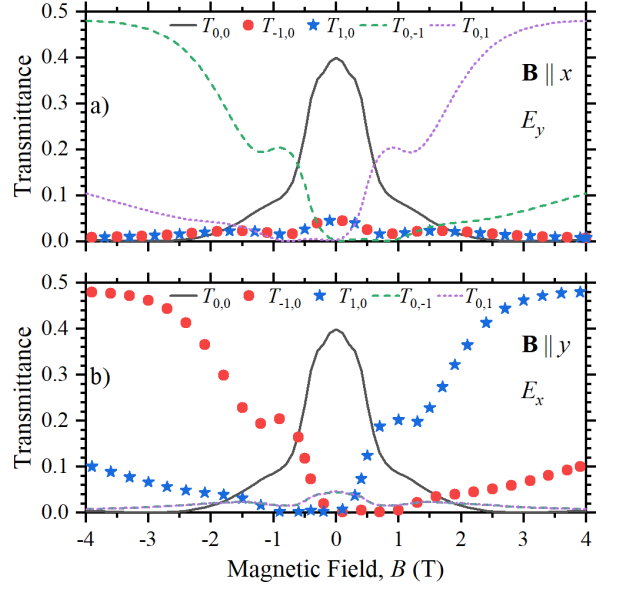


Figure 2: Diffractively transmitted orders for a LP THz wavefront, with $f = 300$ GHz, as function of the externally applied magnetic field amplitude B . Results are comparatively shown for a) $\mathbf{E} \parallel \hat{y}$ (with $\mathbf{B} \parallel \hat{x}$) and b) $\mathbf{E} \parallel \hat{x}$ (with $\mathbf{B} \parallel \hat{y}$). Solid, dashed, and dotted lines are for $T_{0,0}$, $T_{0,-1}$, and $T_{0,1}$, whilst solid circles and stars are for $T_{-1,0}$ and $T_{1,0}$, respectively.

incident wave. First, numerical results for $T_{m,n}$ with $\mathbf{E} \parallel \hat{y}$ and $\mathbf{B} \parallel \hat{x}$ are shown in Figure 2a). The sign of B on the horizontal axis indicates the direction of \mathbf{B} along the

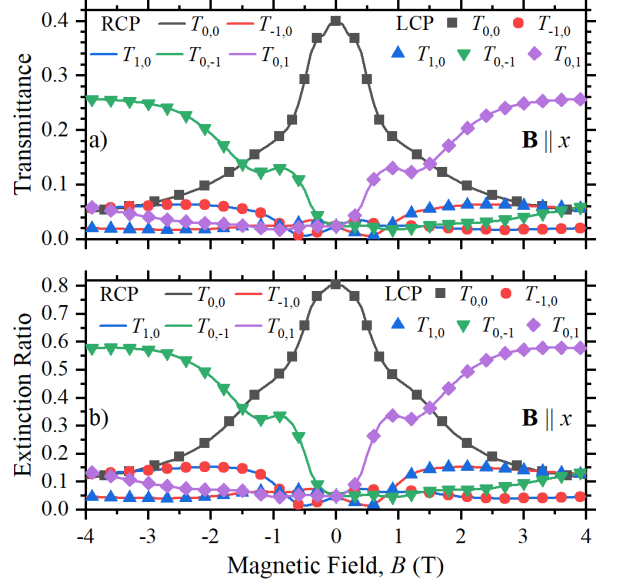


Figure 3: a) Diffractively transmitted orders and b) extinction ratio for a CP THz wavefront, with $f = 300$ GHz, as function of the externally applied magnetic field amplitude B . Solid lines are for RCP, whereas solid symbols are for LCP wavefronts, associated to $T_{0,0}$ (black), $T_{-1,0}$ (red), $T_{1,0}$ (blue), $T_{0,-1}$ (green) and $T_{0,1}$ (purple).

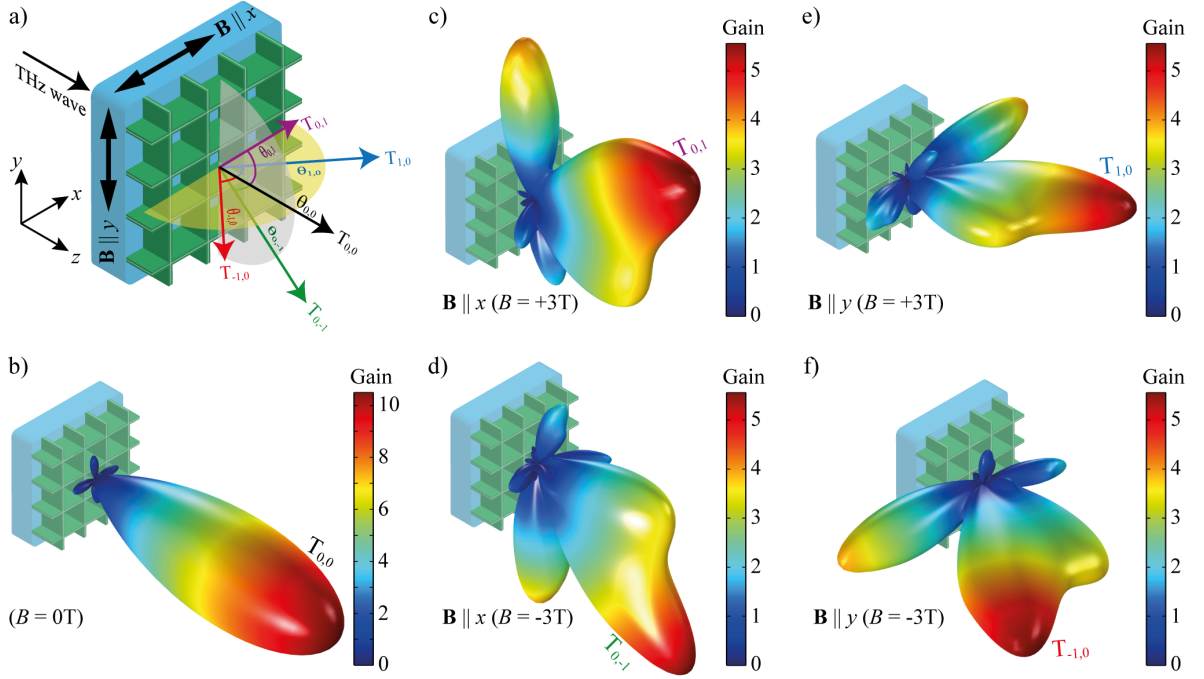


Figure 4: a) Metasurface and the corresponding diffracted beams $T_{n,m}$ are illustrated for eye-guide. The corresponding 3D radiation patterns are plotted for b) $B = 0$ and $B = \pm 3$ T along c)-d) $\pm \hat{x}$ and e)-f) $\pm \hat{y}$ directions.

magnetized axis. The transmission for $B = 0$ is dominated by the diffraction orders ($m = n = 0$) along the z -axis, as observed for $T_{0,0}$ in Figure 2a). Interestingly, transmission becomes increasingly dominated by $T_{0,1}$ and $T_{0,-1}$ along the yz -plane as $\mathbf{B} \neq \mathbf{0} \parallel \hat{x}$ increases. Symmetric results are observed for the xz -plane when the applied magnetic field and electric field polarization are rotated by 90° , as noticed from Figure 2b) for $\mathbf{E} \parallel \hat{x}$ and $\mathbf{B} \parallel \hat{y}$. This behavior is due to the HRI resonances associated with the HMM dispersion of the InSb material, as will be explained later for the more general case of circular polarization (CP).

From here on, CP THz wavefronts are used for a more general discussion. The electric field component of CP waves is written as $\mathbf{E} = (E_x \hat{x} \pm iE_y \hat{y})e^{-ik_{inc}z}$, simultaneously having E_x and E_y components, where the sign \pm denotes the right/left CP (RCP/LCP) state. In analogy to results in Figure 2, we calculated the transmitted diffraction orders $T_{m,n}$ for the RCP and LCP configurations. Numerical results are shown in Figure 3a) for the case of $\mathbf{B} \parallel \hat{x}$, with magnetically induced tilting along the yz -plane. Although not shown here, calculations for $\mathbf{B} \parallel \hat{y}$ exhibited the same symmetry properties discussed in Figure 2b), i.e., transmitted fields tilted along the xz -plane are induced by the external magnetic field. For a quantitative comparison among different transmitted diffracted orders, we calculate the extinction ratio ($ER = T_{m,n}/T_{total}$, where T_{total} is the sum of all transmitted modes) in Figure 3b). From this last figure it can be seen that in the absence of magnetic field ($B = 0$) 81% of the transmitted power corresponds to the $T_{0,0}$ mode.

In contrast, the transmittances $T_{0,\pm 1}$ and $T_{\pm 1,0}$ achieve values as high as 57% of the total transmitted power (as observed from the $ER \approx 0.57$) for the externally applied magnetic field amplitudes $B = \pm 3$ T. Since diffracted transmission is switched from $(0,0)$ to $(\pm 1,0)$ or $(0,\pm 1)$, the corresponding transmitted wavefronts will be deflected

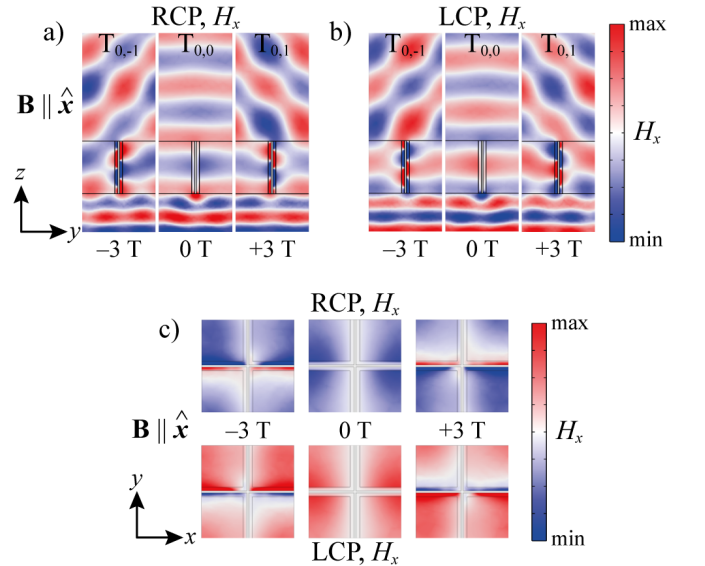


Figure 5: a)-b) Side and c) upper view of H_x near-field profiles for a) RCP and b) LCP incident wavefronts with $B = (-3, 0, +3)$ T along x -axis.

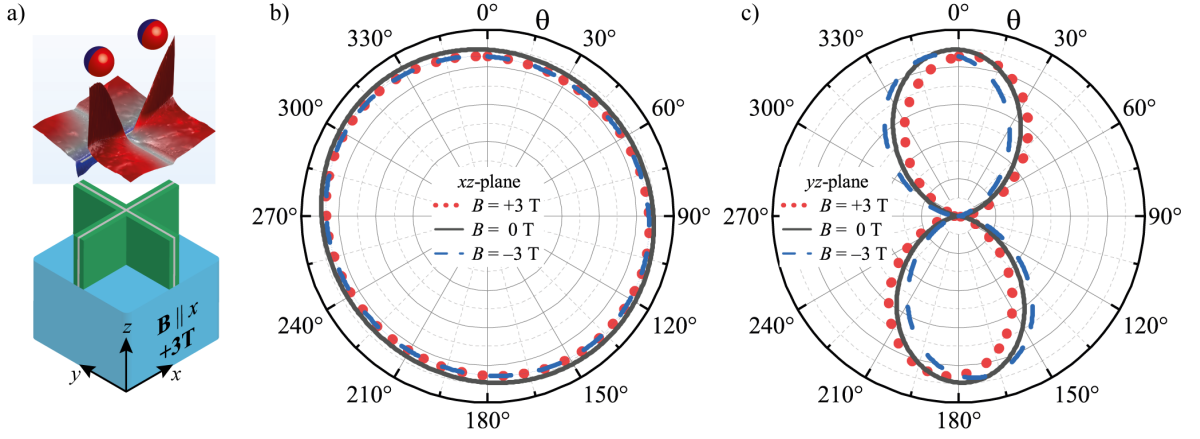


Figure 6: a) Unit cell and its representative dipolar behavior using LCP under $B = +3 \text{ T} \parallel \hat{x}$. Scattered electromagnetic energy along the b) xz and c) yz planes, respectively, for $B = 0 \text{ T}$ (black), $B = +3 \text{ T}$ (red) and $B = -3 \text{ T}$ (blue).

from $\theta_{0,0} = 0^\circ$ (see Eq. (7)) to $\theta_{\pm 1,0} = \theta_{0,\pm 1} = \pm 45^\circ$ by the application of B . Indeed, numerical results for the gain (far-field profile) are shown in Figure 4. For eye-guide, we illustrate the incident direction, cartesian axes, and directions of \mathbf{B} in Figure 4a). Results for $B=0$ and $B = \pm 3 \text{ T}$ along the \hat{x} and \hat{y} directions are shown in Figure 4b)-f). These results can be used for improved sensing⁴ and THz beamforming,^{11,12} where the metasurface can be placed over a transmitter antenna to allow magnetic tuning of the phase array. Moreover, our idea can also find applications in the future Tera-WiFi concept (according to the recent IEEE Standardization 802.15.3d-2017⁴³) for active THz links that communicate a fixed transmission system with at least 5 receiving antennas (see results in Figure 4).

As mentioned before, the magnetically switchable hyperbolic feature of the InSb material is responsible for the tunable THz beamforming in Figure 4. To support this claim, we first plot the near-field profiles for RCP and LCP incident wavefronts in Figure 5a)-c), where numerical results are comparatively shown for $T_{0,-1}, T_{0,0}$, and $T_{0,1}$ with $B = -3 \text{ T}, B = 0 \text{ T}$, and $B = +3 \text{ T}$, respectively. For simplicity, calculations are only shown for $\mathbf{B} \parallel \hat{x}$, since symmetric results are obtained for $\mathbf{B} \parallel \hat{y}$. It can be seen from these figures that an asymmetric dipole resonance is excited for $B = \pm 3 \text{ T}$. The latter is a HRI dielectric resonance occurring only along the \hat{y} -axis, where $\epsilon_\perp > 0$ (perpendicular to \mathbf{B}), whereas the electromagnetic field is mostly expelled from the InSb slabs along the direction where $\epsilon_\parallel < 0$, as noticed from Figure 5c). Indeed, for $\mathbf{B} = 0$, no field is found within the building components of InSb, since both ϵ_\parallel and ϵ_\perp are simultaneously negative.

Having shown the dipole excitation associated with the magnetically switchable hyperbolic behavior of the InSb material, we now qualitatively explain the magnetically active beamforming through the dipole theory. Figure 6a) illustrates (using LCP under $\mathbf{B} = +3 \text{ T} \parallel \hat{x}$) how the resonance in the unit cell can be viewed, in a simplified

form, as two nearby MO dipoles (spheres in the upper side). The external magnetic field (\mathbf{B}) is applied parallel to the axis (\hat{x}) along which the MO dipoles are placed. Figures 6b)-c) show the scattered electromagnetic energy along the xz and yz planes, respectively, from where it can be clearly noticed that magnetically tuned beam tilting is only observed along the plane perpendicular to \mathbf{B} . This tilting occurs due to the magnetically induced

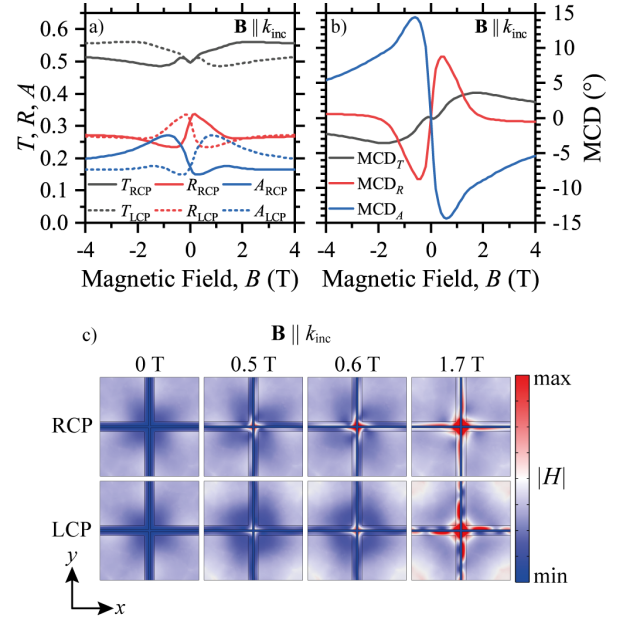


Figure 7: a) Total transmittance (T), reflectance (R) and absorptance (A) as function of $\mathbf{M} \parallel \hat{z}$ for RCP (solid curves) and LCP (dotted curves) at $f = 300 \text{ GHz}$. Magnetically induced differences in the results for RCP and LCP fields resulted in b) MCD for T (black), R (red) and A (blue). c) Normalized near-field profiles (along the xy -plane) for the resonant H -fields of the applied magnetic field amplitude, where magnetically induced chirality (through the Faraday effect) is observed.

dipole moment along the z -axis, as it was demonstrated for a single dipole in Ref. [31]. Although not shown here, we must mention that the number of scattered lobes in the pattern of Figure 6c) depends on the distance between the dipoles. We used here a relatively small distance to illustrate the tilting with only one lobe, whereas additional small lobes can be seen for larger distances. The latter becomes interesting if we see that the patterns in Figure 4 show some minor lobes in several different directions. Nevertheless, a direct comparison cannot be made since the metasurface also has diffractive effects, not included in the qualitative dipole approximation for the unit cell.

Figure 7 shows that the proposed metasurface can also exhibit magnetic circular dichroism (MCD) activity, which occurs when \mathbf{B} is applied parallel to the direction of propagation \mathbf{k}_{inc} ($\hat{\mathbf{z}}$ -axis in this case). Results are shown for the transmittance, reflectance and absorbance with solid and dashed lines for RCP and LCP incident wavefronts, respectively, in Figure 7a). MCD can be defined in transmission, reflection and absorption using the corresponding amplitudes as⁵⁴

$$\text{MCD} = \tan^{-1} \left(\frac{I_{\text{RCP}} - I_{\text{LCP}}}{I_{\text{RCP}} + I_{\text{LCP}}} \right), \quad (25)$$

in degrees ($^\circ$), where I_{RCP} and I_{LCP} are either the transmittance, reflectance, or absorbance amplitudes for the RCP and LCP wavefronts, respectively, with numerical results shown in Figure 7b). Interestingly, since $\mathbf{B} \parallel +\hat{\mathbf{z}}$, HRI dielectric resonances can be excited in the InSb slabs along the xy -plane, as corroborated in Figure 7c), introducing magnetically tunable chirality in the metasurface.

IV. CONCLUSION

We explored the magnetically switchable hyperbolic dispersion of the InSb material, combined with diffractive surfaces and magnetic tilting of scattered fields, to demonstrate a concept for dynamic terahertz beamforming. In

particular, we use the conditions to transmit only the diffracted modes of 0-th and 1-st order, whose diffraction angles can be actively manipulated by the direction and sense of the applied magnetic field. The latter was achieved through the numerical design of the metasurface unit cell. Full-wave numerical results (using the finite element method) were found in qualitative agreement with semi-analytical results from the generalized dipole theory. A proof of concept was conducted using the operating frequency $f = 300$ GHz, which is expected to provide efficient THz indoor wireless communications for future Tera-WiFi networks (according to the IEEE Standardization 802.15.3d-2017). Though results are shown for magnetic field amplitudes of ± 3 T, at temperatures of 200 K, it should be mention that recent experimental demonstrations of high-performance THz isolators (with InSb at room temperature) were made using field amplitudes of up to 0.4 T (which can be supplied by small permanent magnets).^{11,32} Since magnetic field effects can be manipulated faster than temperature effects, our idea provides a new way to develop more rapidly reconfiguring THz metasurfaces.

Acknowledgments

This work was partially supported by RNP, with resources from MCTIC, Grant No.01245.020548/2021-07, under the Brazil 6G project of the Radiocommunication Reference Center (Centro de Referência em Radiocomunicações - CRR) of the National Institute of Telecommunications (Instituto Nacional de Telecomunicações - Inatel), Brazil, and by Huawei, under the project Advanced Academic Education in Telecommunications Networks and Systems, contract No PPA6001BRA23032110257684. We also acknowledge financial support from the Brazilian agencies National Council for Scientific and Technological Development-CNPq (152370/2022-6, 314671/2021-8) and FAPESP (2021/06946-0).

* Electronic address: williamofcarvalho@gmail.com

¹ X. Fu, Y. Liu, Q. Chen, Y. Fu, and T. J. Cui, *Front. Phys.* p. 427 (2022).

² Y. Jiang, G. Li, H. Ge, F. Wang, L. Li, X. Chen, M. Lv, and Y. Zhang, *IEEE Access* (2022).

³ J. M. Jornet, E. W. Knightly, and D. M. Mittleman, *Nat. Commun.* **14**, 841 (2023).

⁴ Q. Wang, Y. Chen, J. Mao, F. Yang, and N. Wang, *Sensors* **23** (2023), ISSN 1424-8220, URL <https://www.mdpi.com/1424-8220/23/13/5902>.

⁵ Y. Luo, Q. Zeng, X. Yan, Y. Wu, Q. Lu, C. Zheng, N. Hu, W. Xie, and X. Zhang, *IEEE Access* **7**, 30802 (2019).

⁶ R. Pant and L. Malviya, *Int. J. Commun. Syst.* p. e5474 (2023).

⁷ Z. Wang, J. Qiao, S. Zhao, S. Wang, C. He, X. Tao, and S. Wang, *InfoMat* **3**, 1110 (2021).

⁸ W. Xu, T. Lv, H. Guo, J. Yang, Y. Bi, Q. Zhang, D. Feng, T. Deng, and X. Li, *Microw. Opt. Technol. Lett.* **63**, 817 (2021).

⁹ C. Chen, M. Chai, M. Jin, and T. He, *Adv. Mater. Technol.* **7**, 2101171 (2022).

¹⁰ Q. Li, X. Cai, T. Liu, M. Jia, Q. Wu, H. Zhou, H. Liu, Q. Wang, X. Ling, C. Chen, et al., *Nanophotonics* **11**, 2085 (2022), URL <https://doi.org/10.1515/nanoph-2021-0801>.

¹¹ Z. Tan, F. Fan, S. Guan, H. Wang, J. Cheng, Y. Ji, and S. Chang, *Adv. Opt. Mater.* p. 2202938 (2023).

¹² X. You, R. T. Ako, M. Bhaskaran, S. Sriram, C. Fumeaux, and W. Withayachumnankul, *Laser Photonics Rev.* p. 2200305 (2023).

¹³ A. G. Davies, E. H. Linfield, M. Pepper, T. W. Crowe, T. Globus, D. L. Woolard, and J. L. Hes-

- ler, *Philos. Trans. R. Soc. A: Mathematical, Physical and Engineering Sciences* **362**, 365 (2004), <https://royalsocietypublishing.org/doi/pdf/10.1098/rsta.2003.1327>, URL <https://royalsocietypublishing.org/doi/abs/10.1098/rsta.2003.1327>.
- ¹⁴ Q. Song, Y. Xu, Z. Zhou, H. Liang, M. Zhang, G. Zhu, J. Yang, and P. Yan, *ACS Photonics* **9**, 2520 (2022), URL <https://doi.org/10.1021/acsp Photonics.2c00735>.
- ¹⁵ N. Yu and F. Capasso, *Nat. Mater.* **13**, 139 (2014), ISSN 1476-4660, URL <https://doi.org/10.1038/nmat3839>.
- ¹⁶ N. Yu, P. Genevet, M. A. Kats, F. Aieta, J.-P. Tetienne, F. Capasso, and Z. Gaburro, *Science* **334**, 333 (2011), <https://www.science.org/doi/pdf/10.1126/science.1210713>, URL <https://www.science.org/doi/abs/10.1126/science.1210713>.
- ¹⁷ S. Taravati and G. V. Eleftheriades, *ACS Photonics* **9**, 305 (2022), URL <https://doi.org/10.1021/acsp Photonics.1c01041>.
- ¹⁸ X. G. Zhang, Y. L. Sun, B. Zhu, W. X. Jiang, Q. Yu, H. W. Tian, C.-W. Qiu, Z. Zhang, and T. J. Cui, *Light Sci. Appl.* **11**, 126 (2022), ISSN 2047-7538, URL <https://doi.org/10.1038/s41377-022-00817-5>.
- ¹⁹ D. Neshev and I. Aharonovich, *Light Sci. Appl.* **7**, 58 (2018), ISSN 2047-7538, URL <https://doi.org/10.1038/s41377-018-0058-1>.
- ²⁰ K. Du, H. Barkaoui, X. Zhang, L. Jin, Q. Song, and S. Xiao, *Nanophotonics* **11**, 1761 (2022), URL <https://doi.org/10.1515/nanoph-2021-0684>.
- ²¹ E. Cortés, F. J. Wendisch, L. Sortino, A. Mancini, S. Ezen-dam, S. Saris, L. de S. Menezes, A. Tittl, H. Ren, and S. A. Maier, *Chem. Rev.* **122**, 15082 (2022), ISSN 0009-2665, URL <https://doi.org/10.1021/acs.chemrev.2c00078>.
- ²² J. Wu, Z. Shen, S. Ge, B. Chen, Z. Shen, T. Wang, C. Zhang, W. Hu, K. Fan, W. Padilla, et al., *Appl. Phys. Lett.* **116**, 131104 (2020), ISSN 0003-6951, https://pubs.aip.org/aip/apl/article-pdf/doi/10.1063/1.5144858/13951162/131104.1_online.pdf, URL <https://doi.org/10.1063/1.5144858>.
- ²³ X. Fu, L. Shi, J. Yang, Y. Fu, C. Liu, J. W. Wu, F. Yang, L. Bao, and T. J. Cui, *ACS Appl. Mater. Interfaces* **14**, 22287 (2022), ISSN 1944-8244, URL <https://doi.org/10.1021/acscami.2c02601>.
- ²⁴ S. Liu, F. Xu, J. Zhan, J. Qiang, Q. Xie, L. Yang, S. Deng, and Y. Zhang, *Opt. Lett.* **47**, 1891 (2022), URL <https://opg.optica.org/ol/abstract.cfm?URI=ol-47-7-1891>.
- ²⁵ X. Zhuang, W. Zhang, K. Wang, Y. Gu, Y. An, X. Zhang, J. Gu, D. Luo, J. Han, and W. Zhang, *Light Sci. Appl.* **12**, 14 (2023), ISSN 2047-7538, URL <https://doi.org/10.1038/s41377-022-01046-6>.
- ²⁶ D. Wang, S. Sun, Z. Feng, and W. Tan, *Opt. Mater. Express* **10**, 2054 (2020), URL <https://opg.optica.org/ome/abstract.cfm?URI=ome-10-9-2054>.
- ²⁷ X. Chen, S. Zhang, K. Liu, H. Li, Y. Xu, J. Chen, Y. Lu, Q. Wang, X. Feng, K. Wang, et al., *ACS Photonics* **9**, 1638 (2022), <https://doi.org/10.1021/acsp Photonics.1c01977>, URL <https://doi.org/10.1021/acsp Photonics.1c01977>.
- ²⁸ Y. Zeng, D. Lu, X. Xu, X. Zhang, H. Wan, J. Wang, X. Jiang, X. Yang, M. Xu, Q. Wen, et al., *Adv. Opt. Mater.* **11**, 2202651 (2023), <https://onlinelibrary.wiley.com/doi/pdf/10.1002/adom.202202651>, URL <https://onlinelibrary.wiley.com/doi/abs/10.1002/adom.202202651>.
- ²⁹ G. H. B. Damasceno, W. O. F. Carvalho, A. J. Cerqueira Sodr e, O. N. J. Oliveira, and J. R. Mej a-Salazar, *ACS Appl. Mater. Interfaces* **15**, 8617 (2023), pMID: 36689678, <https://doi.org/10.1021/acscami.2c19376>, URL <https://doi.org/10.1021/acscami.2c19376>.
- ³⁰ W. O. F. Carvalho, G. H. B. Damasceno, E. Moncada-Villa, and J. R. Mej a-Salazar, *Opt. Lett.* **48**, 680 (2023), URL <https://opg.optica.org/ol/abstract.cfm?URI=ol-48-3-680>.
- ³¹ W. O. F. Carvalho, E. Moncada-Villa, and J. R. Mej a-Salazar, *IEEE Trans. Antennas Propag.* **71**, 7473 (2023).
- ³² S. Lin, S. Silva, J. Zhou, and D. Talbayev, *Adv. Opt. Mater.* **6**, 1800572 (2018), <https://onlinelibrary.wiley.com/doi/pdf/10.1002/adom.201800572>, URL <https://onlinelibrary.wiley.com/doi/abs/10.1002/adom.201800572>.
- ³³ T. Li, F. Fan, Y. Ji, Z. Tan, Q. Mu, and S. Chang, *Opt. Lett.* **45**, 1 (2020).
- ³⁴ F. Fan, D. Zhao, Z. Tan, Y. Ji, J. Cheng, and S. Chang, *Adv. Opt. Mater.* **9**, 2101097 (2021).
- ³⁵ Z. Tan, F. Fan, D. Zhao, Y. Ji, J. Cheng, and S. Chang, *Adv. Opt. Mater.* **9**, 2002216 (2021), <https://onlinelibrary.wiley.com/doi/pdf/10.1002/adom.202002216>, URL <https://onlinelibrary.wiley.com/doi/abs/10.1002/adom.202002216>.
- ³⁶ M. Faraday, *Philos. Trans. R. Soc. Lond.* **136**, 1 (1846), URL <https://doi.org/10.1098/rstl.1846.0001>.
- ³⁷ J. Kerr, *Rep. Brit. Assoc. Adv. Sci* **3**, 321 (1877), ISSN 1941-5982, URL <https://doi.org/10.1080/14786447708639245>.
- ³⁸ J. Kerr, *Lond. Edinb. Dublin Philos. Mag. J. Sci.* **5**, 161 (1878), ISSN 1941-5982, URL <https://doi.org/10.1080/14786447808639407>.
- ³⁹ C. Rizal, M. G. Manera, D. O. Ignatyeva, J. R. Mej a-Salazar, R. Rella, V. I. Belotelov, F. Pineider, and N. Maccaferri, *J. Appl. Phys.* **130**, 230901 (2021), ISSN 0021-8979, https://pubs.aip.org/aip/jap/article-pdf/doi/10.1063/5.0072884/13705827/230901.1_online.pdf, URL <https://doi.org/10.1063/5.0072884>.
- ⁴⁰ M. Kenney, J. Grant, Y. D. Shah, I. Escorc a-Carranza, M. Humphreys, and D. R. S. Cumming, *ACS Photonics* **4**, 2604 (2017), URL <https://doi.org/10.1021/acsp Photonics.7b00906>.
- ⁴¹ B. Jany, K. Szajna, M. Nikiel, D. Wrana, E. Trynkiewicz, R. Pedrys, and F. Krok, *Appl. Surf. Sci.* **327**, 86 (2015), ISSN 0169-4332, URL <https://www.sciencedirect.com/science/article/pii/S0169433214026385>.
- ⁴² W. Li, Z. Liu, X. Zhang, and X. Jiang, *Appl. Phys. Lett.* **100**, 161108 (2012), ISSN 0003-6951, https://pubs.aip.org/aip/apl/article-pdf/doi/10.1063/1.4705084/13582373/161108.1_online.pdf, URL <https://doi.org/10.1063/1.4705084>.
- ⁴³ IEEE Std 802.15.3d-2017, Amendment to IEEE Std 802.15.3-2016 as amended by IEEE Std 802.15.3e-2017 pp. 1–55 (2017).
- ⁴⁴ V. Petrov, T. Kurner, and I. Hosako, *IEEE Communications Magazine* **58**, 28 (2020).
- ⁴⁵ Z. Tan, F. Fan, X. Dong, J. Cheng, and S. Chang, *Sci. Rep.* **9**, 20210 (2019).
- ⁴⁶ H.-J. Hagemann, W. Gudat, and C. Kunz, *J. Opt. Soc. Am.* **65**, 742 (1975).
- ⁴⁷ M. Naftaly and R. E. Miles, *J. Appl. Phys.* **102**, 043517 (2007).
- ⁴⁸ B. Zhou, W. Jia, C. Xiang, Y. Xie, J. Wang, G. Jin, Y. Wang, and C. Zhou, *Opt. Express* **29**, 32042 (2021).
- ⁴⁹ L. Novotny and B. Hecht, *Principles of Nano-Optics* (Cam-

bridge University Press, Cambridge, 2012), 2nd ed.

- ⁵⁰ N. Maccaferri, L. Bergamini, M. Pancaldi, M. K. Schmidt, M. Kataja, S. v. Dijken, N. Zabala, J. Aizpurua, and P. Vavassori, *Nano Lett.* **16**, 2533 (2016).
- ⁵¹ A. Ott, P. Ben-Abdallah, and S.-A. Biehs, *Phys. Rev. B* **97**, 205414 (2018).
- ⁵² R. M. Abraham Ekeröth, A. García-Martín, and J. C. Cuevas, *Phys. Rev. B* **95**, 235428 (2017), URL <https://link.aps.org/doi/10.1103/PhysRevB.95.235428>.
- ⁵³ M. Lobet, N. Kinsey, I. Liberal, H. Caglayan, P. A. Huidobro, E. Galiffi, J. R. Mejía-Salazar, G. Palermo, Z. Jacob, and N. Maccaferri, *New horizons in near-zero refractive index photonics and hyperbolic metamaterials* (2023), 2306.01314.
- ⁵⁴ E. Mohammadi, K. Tsakmakidis, A.-N. Askarpour, P. Dekhoda, A. Tavakoli, and H. Altug, *ACS Photonics* **5**, 2669 (2018).